



Au surface plasmon resonance promoted charge transfer in Z-scheme system enables exceptional photocatalytic hydrogen evolution

Muhammad Humayun^a, Habib Ullah^b, Zhuo-Er Cheng^a, Asif Ali Tahir^b, Wei Luo^{a,*}, Chundong Wang^{a,*}

^a School of Optical and Electronic Information, Wuhan National Laboratory for Optoelectronics, Engineering Research Center for Functional Ceramics of the Ministry of Education, Huazhong University of Science and Technology, Wuhan 430074, People's Republic of China

^b Environment and Sustainability Institute (ESI), University of Exeter, Penryn Campus, Penryn, Cornwall TR10 9FE, United Kingdom

ARTICLE INFO

Keywords:

G-C₃N₄
Porphyrin
Charge transfer
H₂ evolution
Quantum efficiency

ABSTRACT

Highly efficient photocatalytic water reduction to evolve hydrogen can be achieved by the construction of Z-scheme systems that mimics natural photosynthesis. However, coupling appropriate semiconductors with suitable water reduction potential still remains challenging. Herein, we report a novel Z-scheme system, based on the Au decorated 5,10,15,20-tetrakis(4-trimethylammonio-phenyl) porphyrin tetra(p-toluene sulfonate) functionalized iron-doped carbon nitride. We prepared carbon nitride by varying the amount of iron dopant and then functionalized with porphyrin to obtain heterostructure photocatalyst. Owing to the strong interfacial contact and proper band alignment, a Z-scheme system is fabricated. Finally, we deposited Au nanoparticles over the surface of the as-fabricated Z-scheme system to promote the surface redox properties via efficient charge carrier's separation and transfer. The 3Au-3 P/30Fe-CN photocatalyst achieved excellent H₂ evolution activity by producing 3172.20 μmol h⁻¹ g⁻¹ under UV-visible irradiation. The calculated quantum efficiencies for 3Au-3 P/30Fe-CN photocatalyst at 365 and 420 nm irradiation wavelengths are 7.2% and 3.26%, respectively. The experimentally observed efficiency of our photocatalyst is supported by the density functional theory simulations in terms of the lowest work function and strong electrostatic interaction among the constituents of Z-scheme system.

1. Introduction

With global reliance on the non-renewable fossil fuels such as crude oil, coal, uranium, and natural gas and the increasing alarm over their impact on global climate, its urgent to search for alternative clean and renewable energy sources. Semiconductors-based photocatalytic water reduction to evolve H₂ has been regarded as an ideal technique for transforming solar energy into chemical energy (green fuels) [1,2]. Regrettably, majority of the single-component photocatalysts have been proven to be inappropriate for efficient H₂ evolution due to the thermodynamic discrepancy between their optical absorption characteristics and redox potentials. Inspired by natural photosynthesis, an artificial photosynthesis system also called Z-scheme photocatalytic system comprising two dissimilar photocatalysts received marvelous attention for efficient water splitting [3,4]. In such type of photocatalytic systems, photogenerated electrons of the photocatalyst with more positive conduction band (CB) and holes of the photocatalyst with

more negative valence band (VB) recombine at the composite interface. The electrons of the photocatalyst with more negative CB has longer lifetime and reduce protons to generate H₂. Meanwhile, the holes of the photocatalyst with more positive VB take part in oxidation reactions. Thus, Z-scheme photocatalytic systems can provide the required redox power for efficient photocatalysis [5,6].

To construct Z-scheme photocatalytic systems, photocatalysts with proper band alignments must be considered for effective charge transfer at the interfacial contact of fabricated heterostructure [7,8]. Until now, abundant metal oxides-based Z-scheme heterostructure photocatalysts have been reported [9,10]. The polymeric graphitic carbon nitride (g-C₃N₄) has been proven to be an appropriate component for constructing Z-scheme photocatalytic systems owing to its abundant features such as exceptional charge transfer and redox ability, earth abundance, tunable band structure, huge interfacial contact area, high chemical and thermal stability, low cost and suitable band gap (i.e., 2.7 eV) [11]. However, owing to the insufficient solar energy harvesting and

* Corresponding authors.

E-mail addresses: luowei@mail.hust.edu.cn (W. Luo), apcdwang@hust.edu.cn (C. Wang).

<https://doi.org/10.1016/j.apcatb.2022.121322>

Received 23 January 2022; Received in revised form 11 March 2022; Accepted 13 March 2022

Available online 16 March 2022

0926-3373/© 2022 Elsevier B.V. All rights reserved.

rapid charge carrier's recombination, the practical applications of g-C₃N₄ (CN) are still limited. A lot of research has been done to overcome these shortfalls via exfoliation of bulk CN into nanosheets, defect engineering, dye sensitization, and heterostructures construction [12, 13].

The role of transition metal Fe doping in g-C₃N₄ is very important. It is widely reported in the literature [14,15] that nitrogen pots in the heptazine rings of g-C₃N₄ contains six lone-pair electrons which are highly beneficial for bonding with Fe. The resultant Fe-N chemical bonds are quite stable and serve as the catalytic active sites to promote the photocatalytic reactions. Further, Fe doping can significantly promote charge carrier's separation in g-C₃N₄ and optimizes its light absorption which finally enhances its photocatalytic activity.

Recently, porphyrins as superior photosensitizers have been widely employed in photocatalysis due to their excellent chromophore activities over the solar spectrum and exceptional electron donating features owing to their large p-electron systems. Coupling of porphyrins with photocatalysts induce covalent interaction at the margin of porphyrin ring and photocatalyst surface via the different functional groups. These induce covalent bands form channels which enhances charge distribution between the photocatalyst and porphyrin components, leading to the p * orbital delocalization of the porphyrin components [16]. As reported in the literature, [17] Au optimizes the optical absorption and accelerates the charge carrier's separation and transfer in CN-based heterostructures due to the localized surface plasmon resonance induced effect. Thus, we have deposited Au over the surface of the as-fabricated 3 P/30Fe-CN photocatalyst so as to optimize its absorption as well as promote its charge carrier's separation for efficient H₂ evolution reaction.

To the best of our knowledge, there have been several reports on the design of porphyrin/CN heterostructure photocatalysts for applications in photocatalysis [18–20]. However, there have been no previous reports on the design of Au decorated 5,10,15,20-tetrakis(4-trimethylammonio-phenyl) porphyrin tetra(p-toluene sulfonate) functionalized Fe doped g-C₃N₄ as Z-scheme heterostructure photocatalysts.

Herein, we report the design and synthesis of Au decorated porphyrin functionalized iron-doped carbon nitride as a Z-scheme photocatalytic system for H₂ evolution. Owing to the comparatively suitable band gap energy of g-C₃N₄ (2.61 eV) fabricated via the hydrothermal route, different level of iron (Fe) dopant was introduced to shift its VB upward to a certain degree. Then porphyrin as an organic semiconductor component was coupled to fabricate heterostructure photocatalyst. Finally, the surface of the heterostructure was decorated via the various content of Au nanoparticles. A Z-scheme heterostructure was confirmed via the experimental and density functional theory results. The resultant Z-scheme heterostructure photocatalyst produced 3172.20 $\mu\text{mol h}^{-1}\text{g}^{-1}$ of H₂ under UV–visible irradiation and achieved quantum efficiencies of 7.2% and 3.26% at wavelengths 365 and 420 nm, respectively. This work will offer a gateway for fabrication of g-C₃N₄-based highly efficient Z-scheme heterostructure photocatalysts. Furthermore, density functional theory simulations were performed to countercheck the significant efficiency of our experimentally observed photocatalyst. It is observed that our proposed Z-scheme has lowest work function and strong electrostatic interaction among its constituents which validate and confirm our experimental data.

2. Materials and Methods

2.1. Materials

High purity analytical grade reagents were used in this work. Iron nitrate nonahydrate (Fe(NO₃)₃·9 H₂O) and melamine (C₃H₆N₆) precursors were purchased from Sinopharm Chemical Reagent Co., LTD. Gold precursor (HAuCl₄·4 H₂O) was purchased from Shanghai Aladdin Bio-Chem Technology Co., LTD. The 5,10,15,20-tetrakis(4-trimethylammonio-phenyl) porphyrin tetra(p-toluene sulfonate) was purchased from

Sigma Aldrich. Methanol (CH₃OH) and ethanol (C₂H₅OH) was purchased from Tianjin Fengchuan Chemical Reagent Technology Co., LTD. Deionized water used throughout the experiments was obtained from the local deionizer machine.

2.2. Synthesis methods of photocatalysts

The g-C₃N₄ (CN) photocatalyst was fabricated via facile route. In a typical procedure, 5 g of melamine powder was dissolved into 70 ml of deionized water under continuous stirring at 50 °C. The solution was then hydrothermally treated at 180 °C in a 100 ml volume Teflon-lined autoclave for 6 h. The precipitate was then collected via centrifugation while washing with deionized water and ethanol in turn. The precipitate was finally dried at 65 °C and then annealed at 550 °C (5 °C min⁻¹) for 2 h. To fabricate xFe-CN photocatalysts, same procedure was followed, except for “x” mg (x = 10, 20, 30, 40, and 50 mg) of Fe(NO₃)₃·9 H₂O precursor was added to the above melamine solution. To fabricate yP/30Fe-CN photocatalysts, 1 g of the optimized 30Fe-CN photocatalyst was dispersed in 25 ml of “y” M (y = 4 × 10⁻⁴, 3 × 10⁻⁴, 2 × 10⁻⁴, and 1 × 10⁻⁴ M) 5,10,15,20-tetrakis(4-trimethylammonio-phenyl) porphyrin tetra(p-toluene sulfonate) solution prepared in acetylacetone (C₅H₈O₂). The solution was continuously stirred for 48 h and finally centrifuged and dried at 85 °C. To fabricate zAu-3 P/30Fe-CN photocatalysts, the optimized 3 P/30Fe-CN photocatalyst was dispersed under stirring in 80 ml of methanol contained in a beaker and then HAuCl₄·4 H₂O solution containing “z” mass ratio percentage of Au (z = 1%, 2%, 3%, and 4%) with respect to the 3 P/30Fe-CN photocatalyst was added to it. The beaker was fully covered and then an inert atmosphere for photo-reduction reaction was generated via nitrogen gas bubbling for half an hour. The solution was irradiated for 15 min with a 300 W Xe-lamp (wavelength = 200–400 nm) under continuous stirring. The sample was collected via the centrifugation, meanwhile washed with de-ionized water and dried at 65 °C.

2.3. Characterizations

The X-ray diffraction (XRD) pattern of the photocatalysts were examined via the x'pert3-powder, PANalytical B.V., (Netherlands) instrument with monochromatic Cu K α radiation source (λ = 1.5406 Å). The absorption spectra of the photocatalysts were analyzed via the SolidSpec-3700 UV–vis spectro-photometer (Shimadzu, Japan). The spectra of the photocatalysts were calibrated with respect to the BaSO₄ reference. The photocatalysts morphology and microstructure were investigated via the field-emission scanning electron microscope (SEM) ZEISS-G300. The Tecnai-G2-F30 (FEI, USA) outfitted with energy dispersive X-ray spectrometer (EDS) operated at 200 KV was employed for taking the transmission electron microscopy (TEM) and high-resolution TEM (HR-TEM) micrographs. A thermo ESCALAB-250XI (USA) X-ray photo-electron spectrometer (XPS) with monochromatic Al-K α radiation source was employed for elemental chemical analysis of the photocatalysts. The VERTEX-70 Bruker Fourier-transform infrared (FT-IR) spectrometer (Made in Germany) with KBr disc was employed for detection of the surface functional groups of the photocatalysts. A Horiba JobinYvon LabRAM (HR800, France) instrument was employed for analysis of Raman spectra of the photocatalysts. A home-built instrument set up with lock-in amplifier and light chopper (SR830, SR540, USA) was employed for measuring the surface photovoltage (SPV) spectra of the photocatalysts. A FP-6500 fluorescence spectrometer (Made in Japan) was employed for measuring the photoluminescence (PL) spectra of the photocatalysts at 325 nm excitation wavelength. The fluorescence decay spectra were obtained via the FLS-980 (EDINBURGH UK) instrument. A NETZSCH STA-449F3 instrument was employed for thermogravimetric analysis (TGA) of the photocatalysts in air environment with temperature range of 30–800 °C. The Brunauer–Emmett–Teller (BET) surface areas and pores size distribution curves of the photocatalysts were obtained via the N₂ adsorption and desorption

method with the help of Mike 3Flex (USA) instrument. The electron paramagnetic resonance (EPR) signals of Fe specie in the Fe-doped photocatalysts were detected via the Bruker A300 instrument. The photoelectrochemical (PEC) I-t curves, cyclic voltammogram curves, and electrochemical impedance spectroscopy (EIS) Nyquist plots were measured via the CHI-760E (Shanghai, Chenhua) instrument in 1 M Na_2SO_4 electrolyte solution versus the Hg/HgO reference electrode. The electron spin resonance (ESR) spectra measurement performed via the Bruker-a300 instrument.

2.4. Photocatalytic hydrogen evolution

The hydrogen evolution experiments were performed in CEAULIGHT CEL-SPH2N-D9 (Beijing) instrument. A fix amount of the photocatalyst (i.e., 50 mg) was dispersed in a mixture of 80 ml H_2O and 20 ml methanol under stirring. Prior to the UV-visible light irradiation, the system was degassed for half an hour to remove the air and oxygen dissolved in the reaction system. Then, a 300 W Xe-lamp (Beijing, Perfect-light) was used as a radiation source. The hydrogen evolved was

detected via the gas chromatograph (CEAULIGHT-GC-7920) with N_2 as carrier gas and TCD as the detector.

3. Results and discussion

3.1. Fabrication route and structural characterization

A four steps procedure (hydrothermal, wet-chemical, calcination and photo-deposition) was employed to fabricate 3Au-3 P/30Fe-CN heterostructure photocatalyst from melamine, iron nitrate, porphyrin and $\text{HAuCl}_4 \cdot 4\text{H}_2\text{O}$ precursors (Fig. 1a). The scanning electron microscopy (SEM) micrographs of g- C_3N_4 (CN) and Fe-incorporated g- C_3N_4 (xFe-CN) (where, x = 10, 20, 30, 40 and 50 mg of Fe precursor) photocatalysts reveals porous texture (Fig. S1a-f). The SEM micrographs of yP/30Fe-CN (where, y = 4×10^{-4} , 3×10^{-4} , 2×10^{-4} and 1×10^{-4} M porphyrin) photocatalysts confirmed the anchoring of porphyrin (P) clusters over the surface of 30Fe-CN photocatalyst (Fig. S2a-d). Similarly, the SEM micrographs of zAu-3 P/30Fe-CN (where, z = 1, 2, 3, and 4 wt% of Au) heterostructure photocatalysts reveals the distribution of uniform size

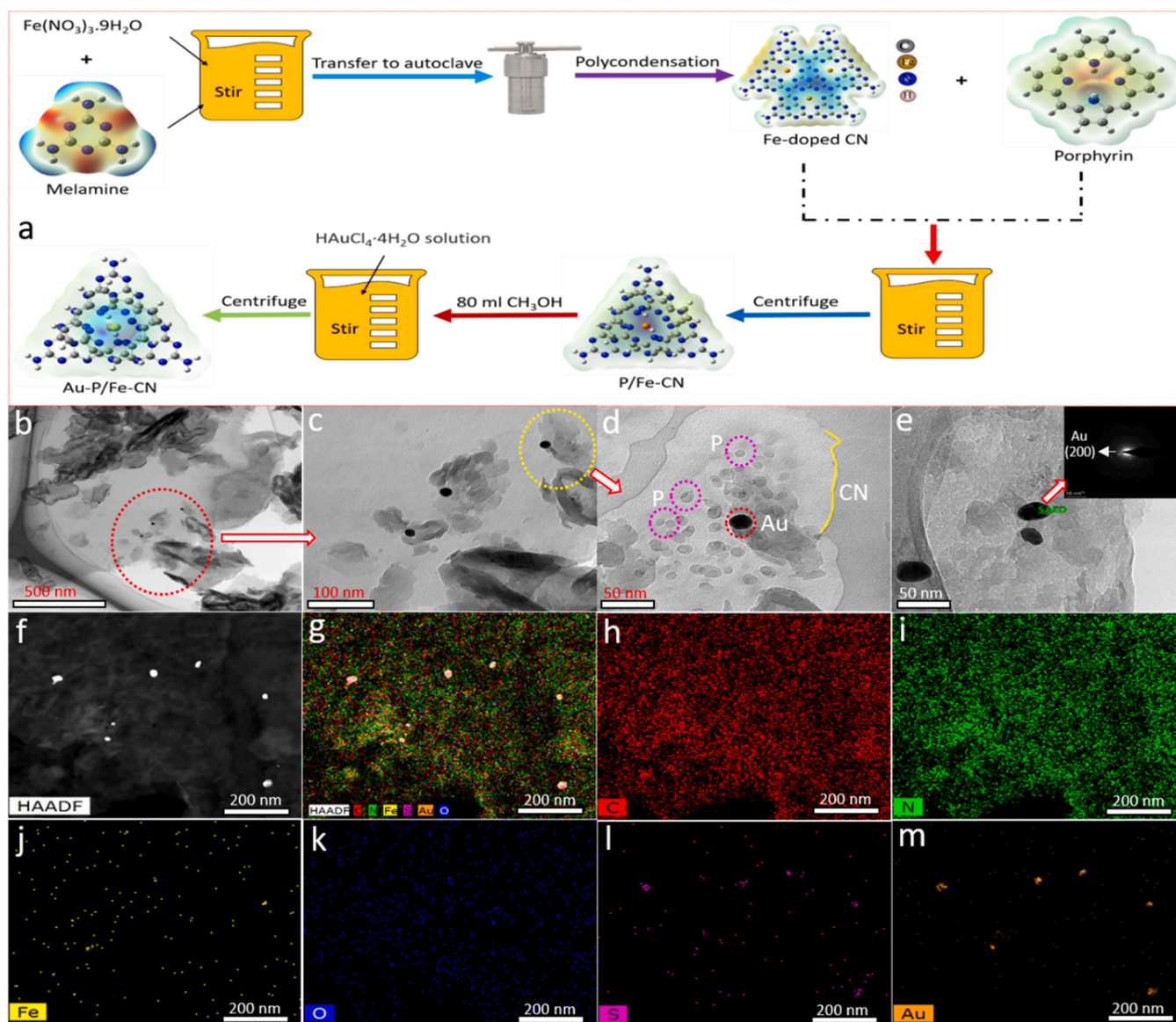


Fig. 1. (a) Scheme for the synthesis of 3Au-3 P/30Fe-CN photocatalyst. (b-d) TEM and HR-TEM micrographs of 3Au-3 P/30Fe-CN photocatalyst. (e) HR-TEM image of the 3Au-3 P/30Fe-CN photocatalyst with inset selected area electron diffraction (SAED) pattern of Au. (f-m) Energy dispersive spectroscopy (EDS) mapping of the 3Au-3 P/30Fe-CN photocatalyst.

Au nanoparticles onto the surface of 3 P/30Fe-CN photocatalyst (Fig. S3a-d). The transmission electron microscopy (TEM) micrograph of CN photocatalyst confirmed the layered nanosheets (Fig. S4a). The high-resolution TEM of CN photocatalyst further confirmed the layered structure (Fig. S4b). The selected area electron diffraction (SAED) confirmed the pattern of CN (Fig. S4c). The energy dispersive spectroscopy (EDS) mapping of CN further reveals the even distribution of carbon and nitrogen elements (Fig. S4d-g). The energy dispersive X-ray (EDX) spectrum of CN photocatalyst shows peaks of carbon and nitrogen elements and their atomic percentage composition is provided as inset (Fig. S4h). After introduction of Fe, the electronic structure of CN didn't change as confirmed by the TEM, HR-TEM micrographs and SAED pattern (Fig. S5a-c). The EDS mapping confirmed the presence of carbon, nitrogen and iron elements in the 30Fe-CN photocatalyst (Fig. S5d-g). The EDX spectrum reveals peaks of carbon, nitrogen and iron elements and their relevant atomic percentage is provided as inset (Fig. S5h). The TEM micrograph of 3 P/30Fe-CN photocatalyst confirmed the presence of P clusters onto the surface of 30Fe-CN photocatalyst (Fig. S6a). The HR-TEM micrograph reveals the distinct layers of P and CN in the 3 P/30Fe-CN photocatalyst (Fig. S6b). The SAED shows the corresponding pattern of CN (Fig. S6c). The EDS mapping of 3 P/30Fe-CN photocatalyst confirmed the presence of carbon, nitrogen, iron, oxygen and sulfur elements (Fig. S6d-j). The TEM and HR-TEM micrographs of 3Au-3 P/30Fe-CN photocatalyst confirmed the successful fabrication of heterostructure (Fig. 1b-d). The SAED further confirmed the pattern of Au nanoparticles in the direction of 200 plane (inset Fig. 1e) [21]. The EDS mapping of 3Au-3 P/30Fe-CN photocatalyst confirmed the distribution of carbon, nitrogen, iron, oxygen, sulfur and gold elements (Fig. 1f-m). It is confirmed that the X-ray diffraction (XRD) pattern of CN exhibit two peaks centering at 27.4° and 13.1° values corresponding to the interlayer stacking of heptazine rings (002) plane and in-plane structural motif of tris-triazine units (100) (Fig. 2a and Fig. S7a) [17]. The (002) peak intensity of CN photocatalyst slightly get weaken with the increase in Fe content. This demonstrate

that Fe forms chemical with nitrogen in the CN host, most likely as it exists in (metallo)porphyrins and (metallo)phthalocyanines (Fig. 2a and Fig. S7a) [22]. The XRD pattern of yP/30Fe-CN photocatalysts reveal that anchoring porphyrin onto the surface of 30Fe-CN didn't change its crystal structure and the XRD peaks of porphyrin didn't appeared in the samples (Fig. 2a and Fig. S7b) [19]. The XRD pattern of zAu-3 P/30Fe-CN photocatalysts reveals distinct peaks of Au at 38.20° , 44.31° , 64.7° , 77.70° and their intensities get stronger with increase in Au content (Fig. 2a and Fig. S7c) [23]. This further confirmed the successful fabrication of zAu-3 P/30Fe-CN heterostructure photocatalysts.

3.2. Band structure

The optical features and band structures of the photocatalysts were further determined via the UV-visible absorption spectroscopy, and UV photo-electron spectroscopy (UPS). The absorption edge of xFe-CN photocatalysts is slightly redshifted in comparison to the pristine CN, demonstrating band gap narrowing with increase in Fe content (Fig. 2b and Fig. S8a). After anchoring P, the Q-bands of P in the range of 500–700 nm also appeared in the yP/30Fe-CN photocatalysts (Fig. 2b and Fig. S8b). This confirmed that strong chemical interaction exists between 30Fe-CN and P photocatalysts. These results are consistent with the previous report [18]. The blue shift in the absorption edge of the yP/30Fe-CN photocatalysts can be ascribed to the wide band gap of porphyrin (Fig. S8d) in comparison to the 30Fe-CN photocatalyst. The surface plasmon resonance (SPR) related peaks can be clearly observed in the zAu-3 P/30Fe-CN photocatalysts (Fig. 2b and Fig. S8c). As determined from the Tauc plots, the intrinsic band gaps of the CN, 10Fe-CN, 20Fe-CN, 30Fe-CN, 40Fe-CN and 50Fe-CN photocatalysts were calculated to be 2.61, 2.6, 2.57, 2.51, 2.51 and 2.53 eV, respectively (Fig. S9a). Similarly, the calculated band gaps of 1 P/30Fe-CN, 2 P/30Fe-CN, 3 P/30Fe-CN, and 4 P/30Fe-CN were predicted to be 2.55, 2.58, 2.58 and 2.60 eV, respectively (Fig. 2c and Fig. S9b). There is no any apparent change in the band gap of 3 P/30Fe-CN photocatalyst

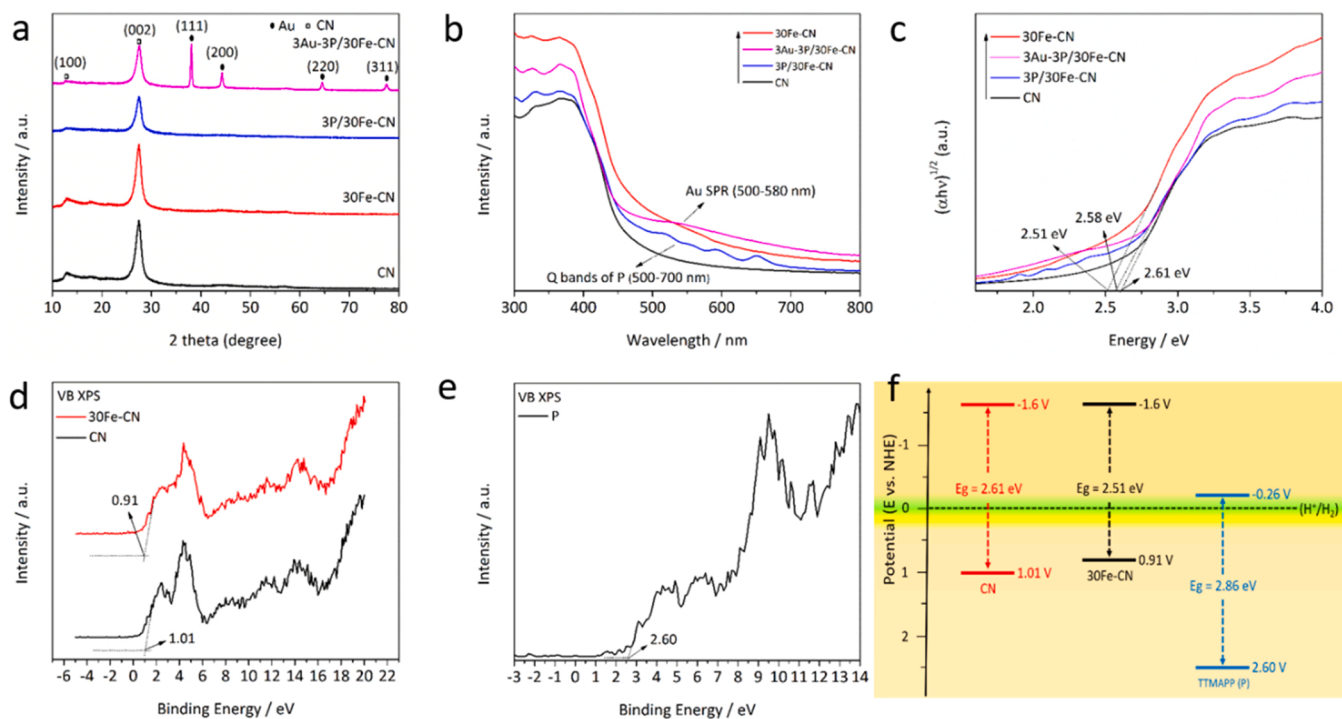


Fig. 2. (a) X-ray diffraction (XRD) patterns, (b) UV-visible absorption spectra and (c) Tauc plots of $(\alpha h\nu)^{1/2}$ vs. photon energy for band gap calculations of CN, 30Fe-CN, 3 P/30Fe-CN and 3Au-3 P/30Fe-CN photocatalysts. Valence band X-ray photoelectron spectroscopy (XPS) spectra (d) of CN and 30Fe-CN photocatalysts and (e) of porphyrin (P). (f) Energy band diagram showing valence and conduction band potential values of CN, 30Fe-CN and P photocatalysts vs. the normal hydrogen electrode (NHE).

after Au deposition (Fig. 2c and Fig. S9c). The calculated band gap of porphyrin was observed to be 2.86 eV (Fig. S9d). As confirmed from the valence band (VB) XPS spectra, the VB maxima of the CN and 30Fe-CN photocatalysts are located at 1.01 and 0.91 V, respectively (Fig. 2d). On the other hand, the VB maximum of porphyrin is located at 2.60 V (Fig. 2e). Thus, knowing the exact band gap values and the obtained VB energy of the single component photocatalysts, their band positions versus the normal hydrogen electrode (NHE) are outlined in Fig. 2f. The Brunauer–Emmett–Teller (BET) surface area of CN, 30Fe-CN, 3 P/30Fe-CN and 3Au-3 P/30Fe-CN photocatalysts were predicted to be 20.39, 25.98, 28.29 and 30.85 m² g⁻¹, respectively (Fig. S10a). Similarly, their pore sizes were estimated to be 3.0, 2.74, 2.2 and 2.76 nm, respectively (Fig. S10b). In fact, there is a slight increase in the BET surface area, suggesting that the activity enhancement is not related to the BET surface areas.

3.3. Chemical composition

The X-ray photoelectron spectroscopy (XPS) survey spectra of CN, 30Fe-CN, 3 P/30Fe-CN and 3Au-3 P/30Fe-CN photocatalysts confirmed the presence of respective elements as labeled (Fig. S11a). The high-

resolution C1s XPS spectra of the photocatalysts exhibit binding energy peaks at 283.3 and 286.6 eV, corresponding to the C=C and C=N structures, respectively (Fig. 3a) [18]. The C1s XPS peaks of 3 P/30Fe-CN photocatalyst are broadened and slightly red shifted which further confirm the existence of a strong chemical interaction between the porphyrin and 30Fe-CN components. The deconvoluted N1s XPS spectrum of CN exhibit three peaks located at 397.17, 398.8 and 402.7 eV, which are attributed to the s-triazine units (i.e., C–N–C and N–C₃) and amino groups (C–N–H), respectively (Fig. 3b) [24]. Likewise, a slight red shift in the N1s XPS peaks of 3 P/30Fe-CN can be observed. The high-resolution Fe2p XPS spectra of 30Fe-CN, 3 P/30Fe-CN and 3Au-3 P/30Fe-CN photocatalysts reveals binding energy peak at 710.25 eV, corresponding to the Fe(III) state of iron (Fig. 3c) [25]. It is worth noting, the Fe atoms are doped at the interstitial site in the tri-s-triazine units as confirmed via the density function theory (DFT) simulations (Fig. 3d). The deconvoluted high-resolution O1s XPS of 3 P/30Fe-CN and 3Au-3 P/30Fe-CN exhibit two prominent peaks at binding energy values of 530.6 and 532.4 eV, corresponding to the lattice oxygen of the functionalized porphyrin and the surface adsorbed oxygen (Fig. 3e). The binding energy peak at 166.6 eV in the high-resolution S2p XPS spectra of 3 P/30Fe-CN and 3Au-3 P/30Fe-CN

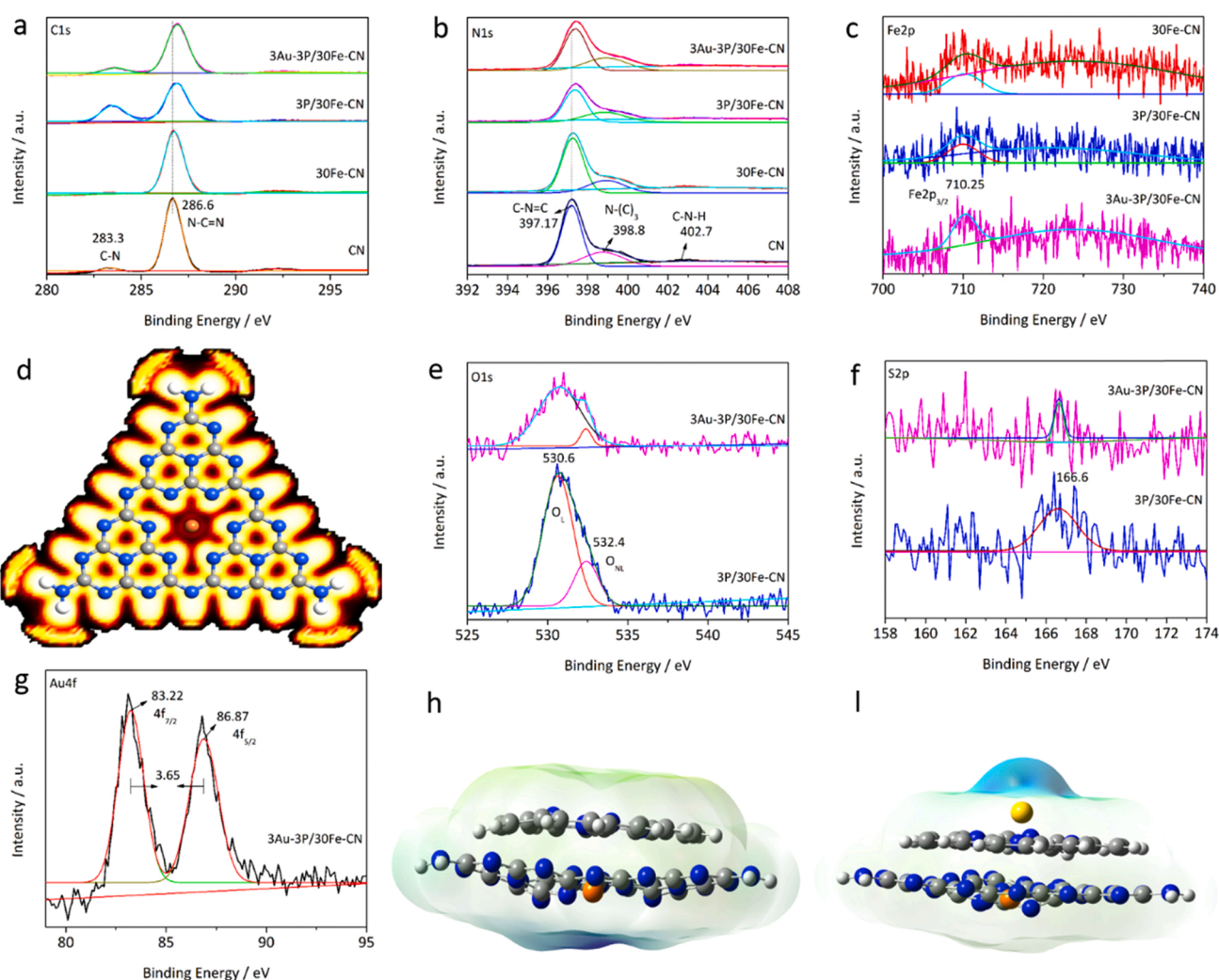


Fig. 3. (a) C1s XPS spectra and (b) N1s XPS spectra of the CN, 30Fe-CN, 3 P/30Fe-CN and 3Au-3 P/30Fe-CN photocatalysts. (c) Fe2p XPS spectra of 30Fe-CN, 3 P/30Fe-CN and 3Au-3 P/30Fe-CN photocatalysts. (d) Interstitial site iron doping in tri-s-triazine unit in case of the 30Fe-CN photocatalyst as confirmed via the density function theory (DFT) simulations. (e) O1s XPS spectra and (f) S2p XPS spectra of 3 P/30Fe-CN and 3Au-3 P/30Fe-CN photocatalysts. (g) Au4f XPS spectra of 3Au-3 P/30Fe-CN photocatalyst. (h) The three-dimensional relaxed geometry of 3 P/30Fe-CN photocatalyst. (i) The three-dimensional relaxed geometry of 3Au-3 P/30Fe-CN photocatalyst.

photocatalysts corresponds to the sulfur element of porphyrin (Fig. 3f). The high-resolution Au4f XPS spectrum of 3Au-3 P/30Fe-CN photocatalyst confirmed the existence of two prominent peaks at 83.22 ($4f_{7/2}$) and 86.87 eV ($4f_{5/2}$), and the difference in their orbital's splitting is 3.65 eV, indicating metallic form of Au nanoparticles (Fig. 3g) [17]. The three-dimensional relaxed geometries of the 3 P/30Fe-CN and 3Au-3 P/30Fe-CN photocatalysts considered for the DFT simulation are depicted in Fig. 3h and Fig. 3i, respectively. The XPS survey spectrum of porphyrin reveals carbon, nitrogen, oxygen and sulfur elements (Fig. S11b). The C1s binding energy peak at 284.5, N1s peaks at 398, 400 and 402.7 eV, O1s peaks at 530.8 and 532.1 eV, and S2p peaks at 166.7 and 168.06 eV corresponds to the porphyrin macrocycle (Fig. S11c-f) [26]. The FT-IR spectra of CN and xFe-CN photocatalysts reveals a prominent peak at 809 cm^{-1} which is the characteristic of bending vibration the tri-s-triazine units. The peaks in the range of $1237\text{--}1634\text{ cm}^{-1}$ can be ascribed to the C–N heterocycles. The broad peak in the range of $3200\text{--}3400\text{ cm}^{-1}$ can be assigned to the surface adsorbed OH[−] and amino groups (Fig. S12a) [27,28]. As clear, the Fe-incorporation didn't change the structure of CN photocatalyst. However, the peak intensity of triazine units slightly decreased after Fe doping as a result of strong interaction between Fe and the nitrogen pots, confirming the Fe–N bond formation [14]. Similarly, the functionalization of porphyrin and photo-deposition of Au nanoparticles didn't change the structure of 30Fe-CN and 3 P/30Fe-CN photocatalysts (Fig. S12b, c). To further investigate the crystalline structure of the photocatalysts, Raman spectroscopy was employed. In fact, Raman spectroscopy is sensitive for detecting the variation in lattice symmetry. The characteristics Raman bands in the range of $470\text{--}1620\text{ cm}^{-1}$ are ascribed to the structural motif of CN (Fig. S13a). The peaks at 477, 750, 981, and 1232 cm^{-1} stem from the stretching vibration modes of CN heterocycles in the graphitic carbon nitride. The Raman band at 707 cm^{-1} is related to the breathing vibration mode of s-triazine rings. The bands located at 1308 and $1407\text{--}1620\text{ cm}^{-1}$ are respectively attributed to the D-band and G-band of CN. Similar characteristic bands

appeared in the xFe-CN photocatalysts, confirming that the incorporation of Fe didn't damage the CN skeleton. However, a slight blue shift in the Raman peaks can be observed and the peaks intensity slightly enhanced. Similarly, the Raman spectra of yP/30Fe-CN photocatalysts reveals that the functionalization of porphyrin didn't influence the structure of 30Fe-CN photocatalyst (Fig. S13b). However, after Au deposition, the Raman peaks intensity of the 3 P/30Fe-CN photocatalyst is apparently decreased suggesting that Au deposition results into the scattering mode of CN photocatalyst (Fig. S13c) [17]. In order to provide conclusive evidence for the presence of Fe(III) sites in the xFe-CN photocatalysts, electron paramagnetic resonance (EPR) analysis was performed. In fact, the EPR spectroscopy gives us valuable information regarding the nature of d⁵ Fe(III) paramagnetic species. As obvious, pristine CN has no EPR signals for Fe(III) ion. Interestingly, the Fe-doped CN photocatalyst has prominent EPR signals of Fe(III) with g values of 4.3 and 2.0 and their peak intensity remarkably enhanced with the increase in Fe content (Fig. 4a) [29].

3.4. Charge separation

To confirm charge carrier's separation in the fabricated photocatalysts, surface photovoltage (SPV) spectroscopy analysis was performed. The SPV technique is highly efficient and non-destructive one primarily employed to investigate the photo-physics of charge carriers in semiconductors and the signal originates from charge separation via the diffusion process. The strong SPV signal elucidate remarkable charge carrier's separation in semiconductors [30,31]. The intensity of the SPV signals of the photocatalysts is in the order of $3\text{Au-3 P/30Fe-CN} > 3\text{ P/30Fe-CN} > 30\text{Fe-CN} > \text{CN}$ (Fig. 4b). Hence, the SPV results confirmed superior charge carrier's separation in the 3Au-3 P/30Fe-CN photocatalyst. Further, the photoluminescence (PL) spectroscopy was employed to investigate the charge carrier's recombination rate in the photocatalysts. The PL spectroscopy is mainly employed to investigate the surface charge recombination, defects, oxygen

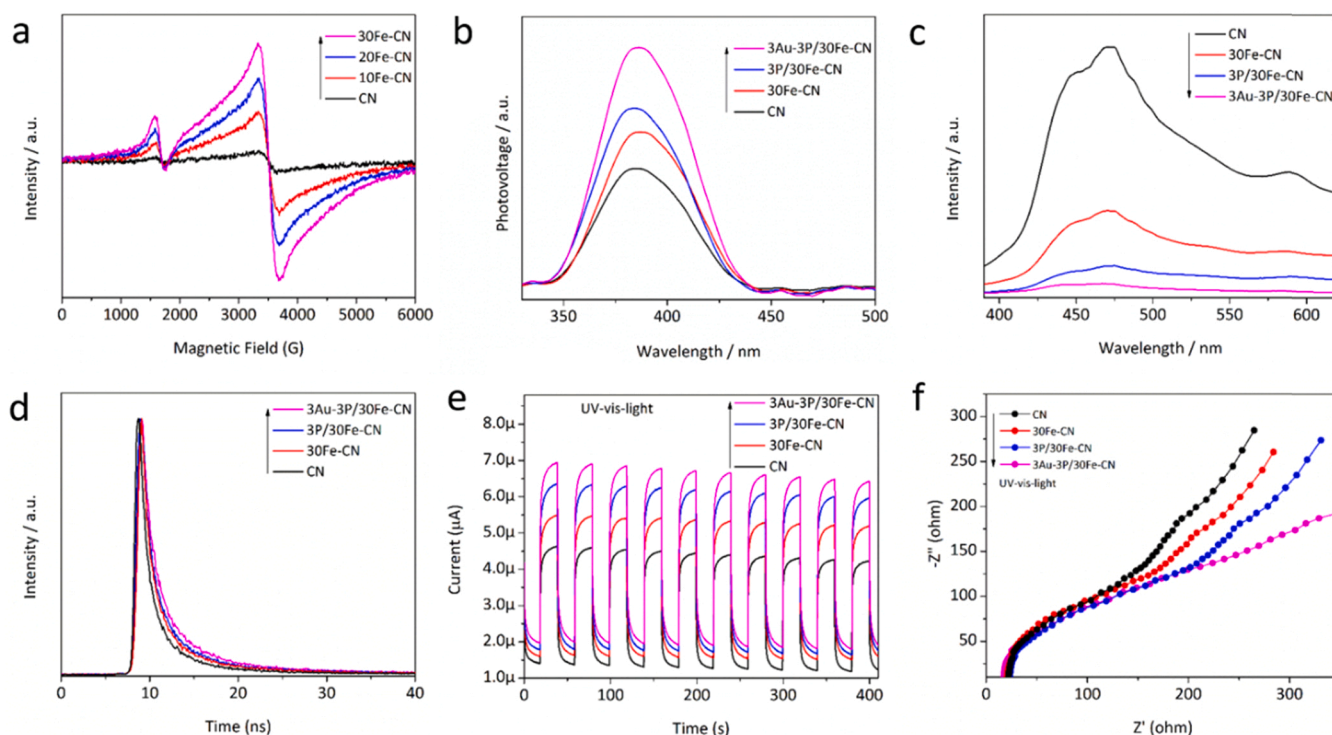


Fig. 4. (a) Electron paramagnetic resonance (EPR) spectra of the CN, 10Fe-CN, 20Fe-CN and 30Fe-CN photocatalysts. (b) Surface photo-voltage (SPV) spectra, (c) photo-luminescence (PL) spectra, (d) time-resolved fluorescence decay spectra, (e) photoelectrochemical (PEC) I-t curves measured in 1 M Na₂SO₄ solution, and (f) electrochemical impedance spectra (EIS) Nyquist plots measured in 1 M Na₂SO₄ solution, of the CN, 30Fe-CN, 3 P/30Fe-CN and 3Au-3 P/30Fe-CN photocatalysts.

vacancies in semiconductors [32,33]. The CN exhibit strong PL signal centering at about 460 nm, which confirm fast charge carrier's recombination. The PL signal of CN is remarkably quenched after incorporation of iron species especially for the 30Fe-CN photocatalyst (Fig. 4c and Fig. S14a). The PL signal of 30Fe-CN photocatalyst is further quenched via porphyrin functionalization especially for the 3 P/30Fe-CN photocatalyst (Fig. 4c and Fig. S14b). A significant quenching in the PL signal of 3 P/30Fe-CN is observed after Au deposition especially for the 3% Au content (Fig. 4c and Fig. S14c). The significant quenching in the PL signal confirms slower charge carrier's recombination rate. The time-resolved fluorescence decay spectra obtained at λ_{ex} of 375 nm further confirmed the photocatalysts charge carrier's lifetime (Fig. 4d). The non-radiative (τ_1) and the radiative (τ_2) processes mainly represent the decay time for faster and slower components. The τ_2 component mainly originate from the indirect self-trapped excitons originated with trapped electron while the τ_1 component originates from the direct generation of free electrons and holes [34,35]. The CN photocatalyst exhibit τ_1 and τ_2 values of 1.52 (Rel% 65.90) and 9.93 (Rel% 34.10) nanosecond (ns). For 30Fe-CN photocatalyst, these values are predicted to be 1.73 (Rel% 61.43) and 11.96 (Rel% 38.57) ns, respectively. The 3 P/30Fe-CN photocatalyst exhibit τ_1 and τ_2 values of 1.89 (Rel% 63.51) and 13.17 (Rel% 36.49) ns, while the 3Au-3 P/30Fe-CN photocatalyst reveals the τ_1 and τ_2 values of 2.25 (Rel% 63.91) and 15.14 (Rel% 36.09) ns. The average lifetimes (τ_{avg}) of CN, 30Fe-CN, 3 P/30Fe-CN and 3Au-3 P/30Fe-CN photocatalysts are 1.96, 2.03, 2.16, and 2.17, respectively. This elucidates that charge carrier's separation in the 3Au-3 P/30Fe-CN photocatalyst has prolong lifetime in comparison to the other photocatalysts. This is due to the fact that electrons of the 30Fe-CN component in the 3Au-3 P/30Fe-CN heterostructure are trapped by the Au nanoparticles due to its superior electrical conductivity. The photoelectrochemical (PEC) *I-t* curves were measured under UV-visible light irradiation in 1.0 M Na₂SO₄ solution versus the Hg/HgO electrode, to further confirm charge separation in the photocatalysts. As obvious, the PEC current response of photocatalysts is in the order of 3Au-3 P/30Fe-CN > 3 P/30Fe-CN > 30Fe-CN > CN (Fig. 4e). This further confirmed superior charge carrier's separation in the 3Au-3 P/30Fe-CN photocatalyst. The electrochemical impedance spectroscopy (EIS) results further confirmed superior charge carrier's separation in the 3Au-3 P/30Fe-CN photocatalyst (Fig. 4f). The thermogravimetric analysis (TGA) of the CN, 30Fe-CN, 3 P/30Fe-CN and 3Au-3 P/30Fe-CN photocatalysts was carried out to confirm the thermal stability of the photocatalysts (Fig. S15). As obvious, the decomposition of pristine CN starts at 600 °C and ends at 750 °C. Notably, the decomposition temperature of 30Fe-CN, 3 P/30Fe-CN and 3Au-3 P/30Fe-CN photocatalysts is lower than that of the pristine CN. Similar results have been obtained in other CN-based heterostructures [36,37]. The shift of weight-loss towards lower temperature might be due to changes in the surface chemistry of CN after modification.

3.5. Hydrogen evolution activities

The photocatalytic experiments for H₂ generation from water/methanol system were performed under visible light and UV-visible light irradiation. As revealed in Fig. S16a, CN produced 9.4 $\mu\text{mol h}^{-1} \text{g}^{-1}$ of H₂ under visible light irradiation. However, after the introduction of Fe into the lattice of CN, H₂ evolution activity is obviously improved and the 30Fe-CN photocatalyst produced 49.5 $\mu\text{mol h}^{-1} \text{g}^{-1}$, which is almost 5.2-fold enhanced compared to the bare CN photocatalyst. From Fig. S16b, it can be seen clearly that after coupling porphyrin, the H₂ evolution activity of the 30Fe-CN photocatalyst is remarkably promoted. Notably, the 3 P/30Fe-CN photocatalyst produced 166.0 $\mu\text{mol h}^{-1} \text{g}^{-1}$ of H₂, which is approximately 17.6 and 3.35-fold enhanced compared to that of the pristine CN and the 30Fe-CN photocatalysts, respectively. In addition, the surface decoration of 3 P/30Fe-CN photocatalyst via the Au nanoparticles significantly promoted the H₂ evolution activity under visible light irradiation. As revealed in Fig. S16c. The amount optimized

3Au-3 P/30Fe-CN photocatalyst produced 384.2 $\mu\text{mol h}^{-1} \text{g}^{-1}$ of H₂, which is comparatively higher than those of the reference photocatalysts. The stability of the 3Au-3 P/30Fe-CN photocatalyst was assessed by the photocatalytic recyclable test under visible light irradiation as revealed in Fig. S16d. The photocatalyst showed stable H₂ evolution during the four successive photocatalytic recycles under visible light irradiation, which confirms its high stability.

The photocatalytic experiments of the photocatalysts were also evaluated under UV-visible light irradiations. The pristine CN produced 39.69 $\mu\text{mol h}^{-1} \text{g}^{-1}$ of H₂ gas, while the xFe-CN photocatalysts exhibited high performance for H₂ production especially the optimized 30Fe-CN photocatalyst with H₂ production rate of 533.29 $\mu\text{mol h}^{-1} \text{g}^{-1}$ (Fig. 5a and Fig. S17a). The H₂ production over the yP/30Fe-CN photocatalysts is considerably high and the optimized 3 P/30Fe-CN photocatalyst produced 1208.08 $\mu\text{mol h}^{-1} \text{g}^{-1}$ (Fig. 5a and Fig. S17b). Interestingly, the zAu-3 P/30Fe-CN photocatalysts revealed superior performance with 3172.20 $\mu\text{mol h}^{-1} \text{g}^{-1}$ of H₂ generation over the optimized 3Au-3 P/30Fe-CN photocatalyst (Fig. 5a and Fig. S17c). This superior photoactivity is ascribed to the exceptional charge transfer and separation between the component systems which is fully supported by the charge transfer results. The photocatalytic performance of the optimized CN, 30Fe-CN, 3 P/30Fe-CN and 3Au-3 P/30Fe-CN photocatalysts were also evaluated under 365 and 420 nm excitation wavelengths for 4 h (Fig. 5b). At 365 nm excitation wavelength, the amount of H₂ produced over the mentioned photocatalysts was 6.4, 8.65, 10.55, and 20.59 μmol , respectively. Similarly, at 420 nm excitation wavelength, the amount of H₂ produced was 4.15, 5.76, 6.52, and 10.57 μmol , respectively. The quantum efficiency for H₂ generation over the 3Au-3 P/30Fe-CN photocatalyst under single wavelengths (i.e., 365 and 420 nm) excitation were predicted to be 7.2% and 3.26%, respectively. The photocatalytic recyclable test for H₂ production over the 3Au-3 P/30Fe-CN was evaluated under UV-visible light irradiation (Fig. S17d). The heterostructure photocatalyst do not exhibit any apparent decrease in the photoactivity even after four recycles. This confirms the excellent photostability of the newly designed heterostructure photocatalyst. In order to further confirm the excellent photoactivity and stability of the 3Au-3 P/30Fe-CN photocatalyst, electrochemical cyclic voltammetry (CV) curves for HER were measured. The CV curves of the optimized CN, 30Fe-CN, 3 P/30Fe-CN and 3Au-3 P/30Fe-CN photocatalysts were conducted in 1 M Na₂SO₄ solution with scan rates of 20 and 50 mV sec⁻¹ in the potential range of 0.0–1.0 V versus Hg/HgO electrode. Among all the electrodes, the 3Au-3 P/30Fe-CN exhibits the highest redox current peak indicating significant electrochemical performance (Fig. S18a-d). Interestingly, at higher scan rate (i.e., 50 mV sec⁻¹) the redox current signals also increase. The 3Au-3 P/30Fe-CN heterostructure electrode presented larger integrated areas in the CV curves in comparison to the other electrodes signifying the remarkably improved specific capacity.

3.6. First principles studies

Initially, three different types of models were employed for the density-functional-theory (DFT) simulations. The DFT calculations are performed on Quantum-ATK [38] and the results are visualized on VESTA and VNL Version 2019.12 [38]. The proposed models were constructed from both single layer and bulk CN. In case of model-1, we used single layer of CN and then interstitially doped it with one Fe atom (denoted by 30Fe-CN), followed by adsorption of porphyrin (denoted as 3 P) and finally one gold atom (denoted by 3Au) is attached on the top of 3 P (Fig. S19 and S20). In order to construct model-2, similar combination of 30Fe-CN and 3 P are used, however, instead of one gold atom, we used a single layer of gold atoms (Fig. S21). In the case of model-3, we used bulk CN, doped with iron (30Fe-CN), followed by the subsequent adsorption of single layers of 3 P and 3Au (Fig. S22). The purpose of these models is to investigate the effect of bulk and single layer of CN and Au. The geometries of the above systems were optimized at the generalized gradient approximation (GGA) with the help of

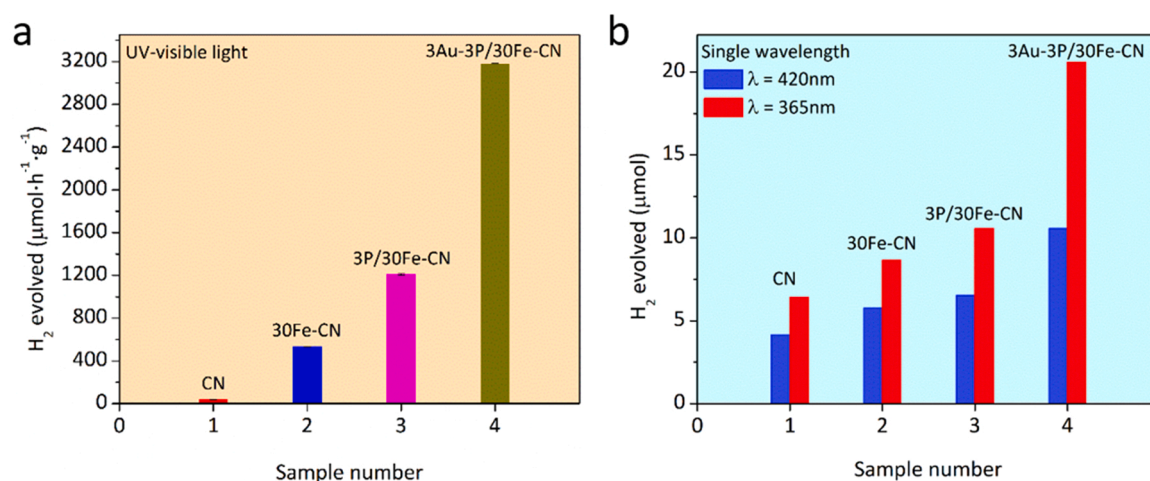


Fig. 5. (a) Photocatalytic H_2 evolution activity under UV-visible irradiation, and (b) photocatalytic H_2 evolution activity under single wavelengths excitation (i.e., 365 and 420 nm) of CN, 30Fe-CN, 3 P/30Fe-CN and 3Au-3 P/30Fe-CN photocatalysts.

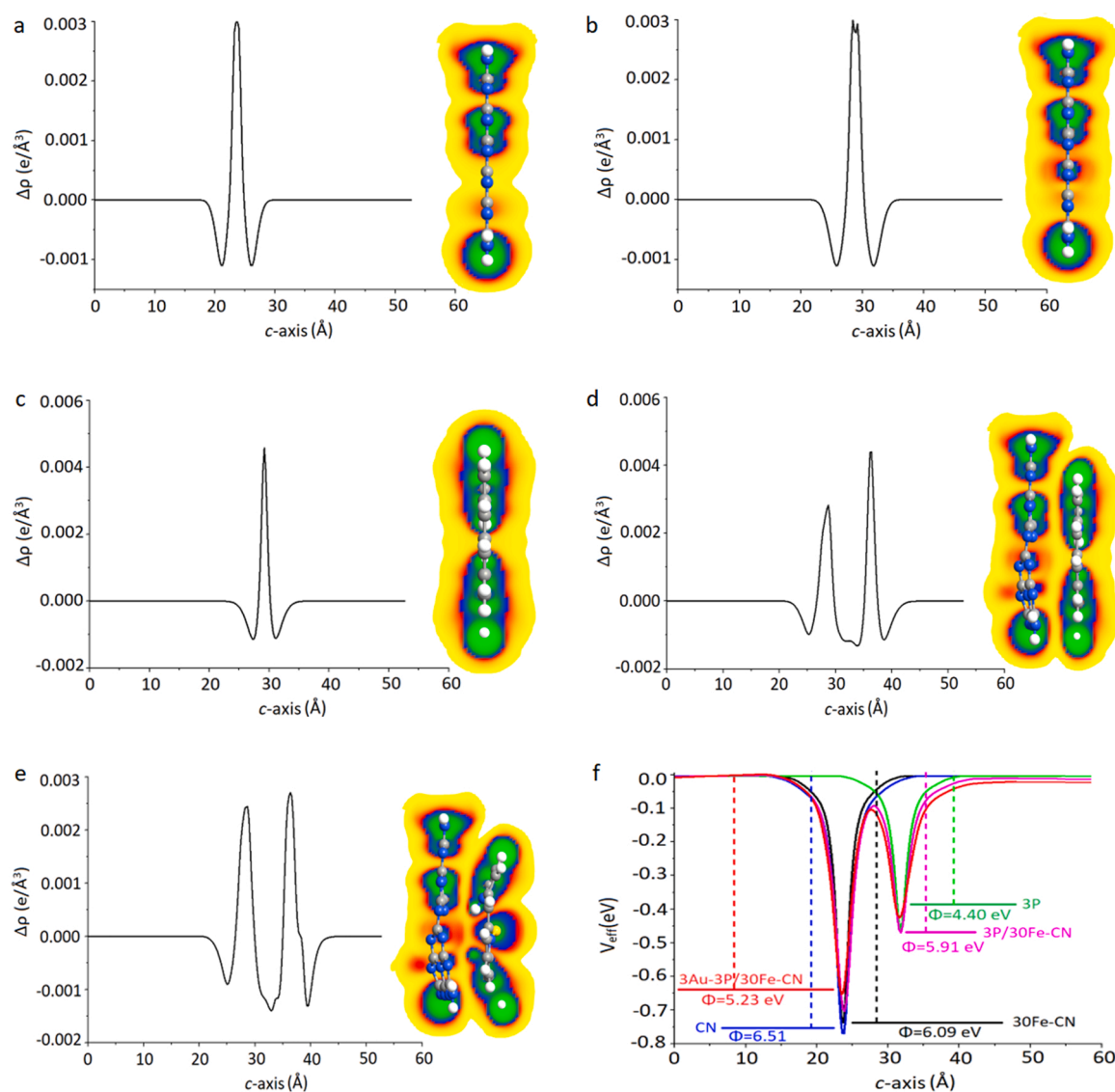


Fig. 6. Two-dimensional (2D) plots of the electron density difference (EDD) of CN, 30Fe-CN, P, 3 P/30Fe-CN and 3Au-3 P/30Fe-CN samples along with their Fermi level (ELF) map (a-e). Combined effective potential map of the investigated models along with their work function (f).

Perdew-Burke-Ernzerh of (PBE) exchange-correlation functional along with Pseudo Dojo pseudopotential. The linear combination of atomic orbitals (LCAO) method is employed for N, C, Au, and H atoms. A $5 \times 1 \times 1$ Monk horst-Pack k-grid and 1200 eV cutoff energy is employed for the single species while, a $5 \times 5 \times 5$ k-point mesh is utilized for the bulk system. Electrostatic potential, electron-difference-density (EDD), partial density of states (PDOS) and effective potentials are simulated at the above-mentioned method. Comparative analyses of the above three models led us to predict that model-1 is computationally convenient and can reproduce the experimental data (vide supra). It is already confirmed that interstitial doping of Fe in CN is ideal compared to the substitution of either C and N atoms. From the partial density of state (PDOS) of the 3Au-3 P/30Fe-CN photocatalyst (Fig. S23), we can see strong hybridization among the CN, Fe, P, Au orbitals. The upper portions of the VB and CB of 3Au-3 P/30Fe-CN photocatalyst are majorly composed of the hybridized orbitals of CN and P (Fig. S23). While the lower density of states areas VB and CB are equally constituted by bonding and anti-bonding orbitals of Fe and Au atoms, respectively. As discussed above, both Au and Fe have larger atomic-radii and higher valency state, which cannot easily fit with C and/or N atoms. Some extra bands can be observed near the Fermi level, which are due to the partially hybridized orbitals of Fe and Au atoms (Fig. S23). The resultant extra bands are due to the dangling or unhybridized Fe orbitals. However, the density of states of Au and Fe atoms are larger in the VB compared to the CB. So, an overall strong hybridization and enhanced density of states are observed at both the CB and VB of the 3Au-3 P/30Fe-CN photocatalyst which confirms its enhanced stability and long-term catalytic activity. Thus, this strong overlapping is responsible for an efficient photocatalytic hydrogen production.

In order to check the interaction of constituents in making our proposed Z-scheme 3Au-3 P/30Fe-CN photocatalyst, the EDD and effective potentials are simulated (Fig. 6 and Fig. S24 and Fig. S25). In case of the 30Fe-CN photocatalyst, the EDD increases along the c-axis (Fig. 6a and b). The electron cloud density distribution of the 3 P is similar to that of CN, however, upon their combination (3 P/30Fe-CN), the P withdraw electronic cloud density from 30Fe-CN. The electronic density of pure 3 P is about $0.005 \text{ e}/\text{\AA}^3$ which is decreased to $0.003 \text{ e}/\text{\AA}^3$ (Fig. 6c and d). This means that the P becomes more negative in 3 P/30Fe-CN system compared to the pristine 3 P. So, electrons are withdrawn from the 30Fe-CN photocatalyst.

Finally, high electronegativity is observed over the surface of 3Au-3 P/30Fe-CN photocatalyst, where the EDD of the positive side of y-axis further decreased to less than $0.003 \text{ e}/\text{\AA}^3$ (Fig. 6e). So, this overall nucleophilic behavior of 3Au-3 P/30Fe-CN validates and confirms its excellent photocatalytic water reduction ability for hydrogen production. For comparison, we have also simulated the effective potentials of the investigated models (Fig. S24 and S25). Moreover, the EDD map of 3Au-3 P/30Fe-CN clearly shows the electron transfer from 3 P/30Fe-CN to Au atoms. This electron transferring phenomena is observed in electrostatic potential (ESP) and effective potential maps as well, where charge accumulate over the surface of Au atoms. So, Au becomes more electronegative and causes the reduction of water that finally produce H_2 as a fuel. The work function of the above photocatalysts was calculated with the help of Eq. (1).

$$\Phi = E_{\text{vac}} - E_F \quad (1)$$

The work functions of CN, 30Fe-CN, P, 3 P/30Fe-CN and 3Au-3 P/30Fe-CN photocatalysts are 6.51, 6.09, 4.40, 5.91, 5.23 eV, respectively (Fig. 6f). Comparative analyses of the work functions of these species led us to conclude that the addition of Fe atom, P, and Au significantly decrease the work function that consequently improve the photoinduced charge carrier's mobility across the interface of the newly designed photocatalyst. Specifically, the work functions of 3 P/30Fe-CN and 3Au-3 P/30Fe-CN are decreased from 6.51 eV (CN) to 5.91 and 5.23 eV, respectively. In addition, the ESP maps of these photocatalysts are also

simulated where 3Au-3 P/30Fe-CN has the lowest potential well compared to the other photocatalysts (Fig. S26).

3.7. Mechanism analysis

It is necessary to carefully investigate the charge transfer mechanism which is the key step in photocatalysis. In semiconductor photocatalysis, the electrons transfer behavior typically relies on the work functions and the energy band structures of the photocatalysts [39]. As the band gaps of the CN, 30Fe-CN, and 3 P photocatalysts were predicted from the Tauc plots which are 2.61, 2.51, and 2.86 eV, respectively. The valence band potentials of the CN, 30Fe-CN and 3 P photocatalysts were obtained from the VB XPS analysis which are 1.01, 0.91, and 2.60 V, respectively. According to the band gap equation; $E_g = E_{\text{VB}} - E_{\text{CB}}$ (where E_{VB} is the VB potential, and E_{CB} is the CB potential vs. the NHE, respectively [40]. Since the E_g and E_{VB} values of the photocatalysts are known, hence the E_{CB} values of the photocatalysts can be calculated via the equation $E_{\text{CB}} = E_g - E_{\text{VB}}$. Herein, the E_{CB} values of CN, 30Fe-CN, and 3 P photocatalysts are predicted to be -1.6 , -1.6 , and -0.26 V, vs. the NHE, respectively. Based on the above values, a Z-scheme charge transfer mechanism in the 3Au-3 P/30Fe-CN photocatalyst is proposed (Fig. 7). In order to further validate the designed Z-scheme system, we have carried out electron spin resonance (ESR) analysis for determination of the reactive intermediates in the photocatalytic reaction system. During the experiment, 5,5-Dimethyl-1-pyrroline N-oxide (DMPO) was used as a spin trap agent for trapping the $\bullet\text{OH}$ and $\bullet\text{O}_2^-$ radicals which produce the adducts of DMPO- $\bullet\text{OH}$ and DMPO- $\bullet\text{O}_2^-$ in reaction medium. The ESR signals of the DMPO- $\bullet\text{OH}$ adduct in the presence of CN, 30Fe-CN, 3 P/30Fe-CN, and 3Au-3 P/30Fe-CN photocatalyst after irradiation for 5 min are revealed in Fig. S27a. As obvious, the CN and 30Fe-CN photocatalysts do not exhibit any ESR signal for the DMPO- $\bullet\text{OH}$ adduct due to their inappropriate valence band potentials for $\bullet\text{OH}$ generation. However, the 3 P/30Fe-CN and 3Au-3 P/30Fe-CN photocatalysts revealed strong signals of the DMPO- $\bullet\text{OH}$ adduct. Similarly, Fig. S27b reveals the ESR signals of the DMPO- $\bullet\text{O}_2^-$ adduct in the presence of CN, 30Fe-CN, 3 P/30Fe-CN, and 3Au-3 P/30Fe-CN photocatalyst after irradiation for 5 min. Interestingly, all of the photocatalysts revealed signals of the DMPO- $\bullet\text{O}_2^-$ adduct demonstrating their suitable conduction band potential for oxygen reduction. Based on these results, it is concluded that the 3 P/30Fe-CN and 3Au-3 P/30Fe-CN photocatalysts simultaneously produced the DMPO- $\bullet\text{OH}$ and DMPO- $\bullet\text{O}_2^-$ adducts in the reaction medium, which strongly validate the designed Z-scheme charge transfer mechanism.

Hence, it is demonstrated that when the 3 P is functionalized with 30Fe-CN photocatalyst, a heterostructure photocatalyst is formed. Since there is a large potential gap between the highly negative CB of 30Fe-CN photocatalyst (i.e., -1.6 V) and less negative CB of 3 P photocatalyst (i.e., -0.26 V), the photogenerated electron of 30Fe-CN can't directly transfer to the CB of 3 P photocatalyst. But instead, the excited electrons in the CB of 3 P and the induced holes in the VB of 30Fe-CN photocatalyst would probably recombine while leaving the excited electrons in the CB of 30Fe-CN and holes in the VB of 3 P photocatalysts. In this way, the charge carrier's lifetime in the 30Fe-CN photocatalyst would remarkably enhance leading to the superior water reduction to evolve H_2 . Thus, the charge transfer in the fabricated heterostructure photocatalyst would proceed in a Z-scheme direction. In order to improve the reduction ability of the designed photocatalyst, we have photo-deposited Au nanoparticles over the surface of the as fabricated 3 P/30Fe-CN heterostructure photocatalyst. In case of the 3Au-3 P/30Fe-CN photocatalyst, under UV-visible irradiation, the built-in electric field induced via the Au surface plasmon resonance (SPR) effect could facilitate charge carrier's separation in the heterostructure. As reported earlier, [30] Au has a work function of 5.1 eV, which is lower than the predicted work function of 3 P/30Fe-CN photocatalyst (i.e., 5.91 eV). Comparative analyses of the work functions values (Fig. 6f) led us to predict that charge transfer can smoothly occur from 3 P/30Fe-CN

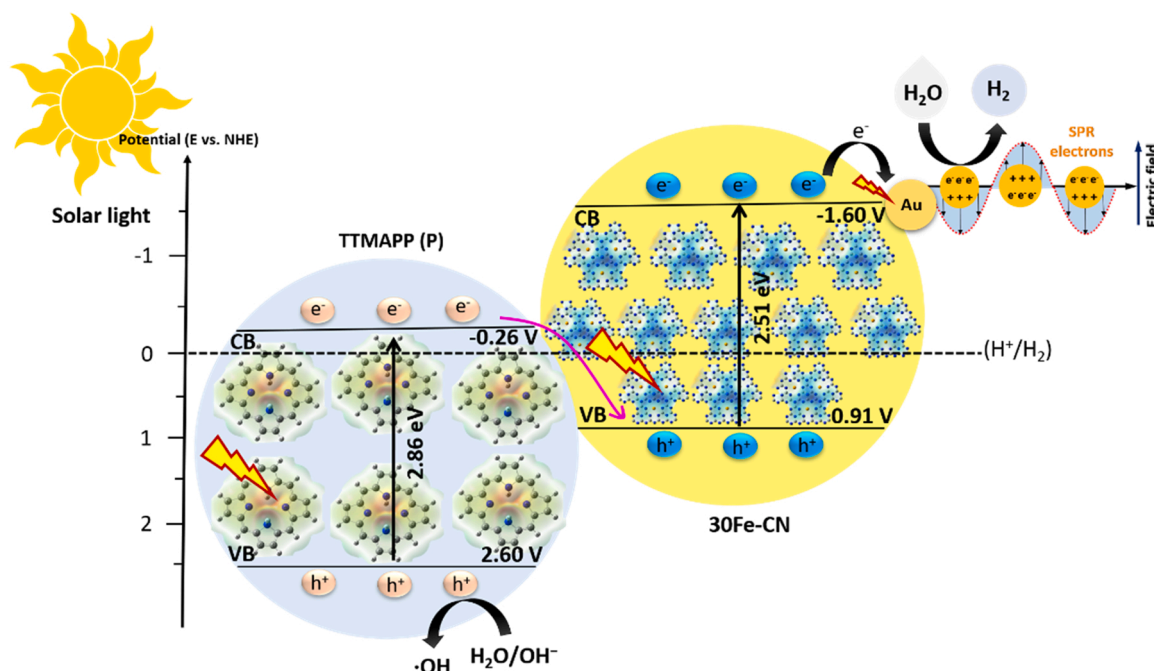


Fig. 7. Scheme for charge transfer and separation and the surface redox reactions over the 3Au-3 P/30Fe-CN photocatalyst.

composite to Au surface. Upon Au deposition onto the surface of 3 P/30Fe-CN, the work function of the 3Au-3 P/30Fe-CN heterostructure is reduced to 5.23 eV which is in-between the work function values of Au and 3 P/30Fe-CN components. This optimum work function of the resulting heterostructure photocatalyst reveals inter-charge transferring in the 3Au-3 P/30Fe-CN photocatalyst that consequently reduces the Fermi level. This statement can be further supported by the electron difference density (EDD) distribution, where the electron density of the 3Au-3 P/30Fe-CN heterostructure photocatalyst is decreased (Fig. 6e). The tightly deposited Au nanoparticles onto the surface of 3 P/30Fe-CN photocatalyst would act as electron traps to enhance charge carrier's separation in the heterostructure photocatalyst due to the superior electrical conductivity of Au nanoparticles. This would lead to the superior performance for photocatalytic water reduction to evolve H_2 . In brief, the photoexcited electrons of 30Fe-CN photocatalyst transferred to the Au surface would proceed water reduction to evolve H_2 , while VB holes of 3 P photocatalyst would proceed water oxidation reactions. Thus, the experimentally and theoretically predicted band levels of the heterostructure photocatalyst have strong correlation and well satisfy the Z-scheme charge transfer mechanism.

4. Conclusion

In summary, we have successfully fabricated Au decorated porphyrin functionalized Fe-doped g-C₃N₄ heterostructure photocatalyst and employed in photocatalysis for H_2 generation from water/methanol system. Based on the experimental and DFT results, a Z-scheme charge transfer mechanism is confirmed. The optimized 3Au-3 P/30Fe-CN photocatalyst revealed superior performance for water reduction to evolve H_2 with a rate of $3172.20 \mu\text{mol h}^{-1} \text{g}^{-1}$ under UV-visible irradiation. Further, the photocatalyst exhibits high quantum efficiencies of 7.2% and 3.26% under excitation wavelengths of 365 and 420 nm, respectively. Besides, the photocatalyst reveals promising recycling stability after 16 h of 4 continuous photocatalytic recyclable tests. This superior photoactivity is ascribed to the exceptional charge carrier's separation and robust surface redox ability donated by the Au SPR and porphyrin components. This work not only provides a new strategy for constructing highly efficient g-C₃N₄-based Z-scheme system, but also affords a valuable model for other semiconductors-based Z-scheme

heterostructures for clean energy production.

CRediT authorship contribution statement

M.H. and Z.C. carried out the synthesis, characterization, photo-electrochemical, electrochemical and photoactivity measurements. H.U. and A.A.T. performed DFT simulations. M.H. wrote the paper. W.L. and C.D.W. conceived the idea and supervised the project. All the authors discussed the results and commented on the manuscript.

Declaration of Competing Interest

The authors declare no conflict of interest.

Acknowledgements

The work was financially supported by the Ministry of Science and Technology of China (Grant No. 2018YFA0702100), the National Natural Science Foundation of China (Grant No. 11874169, 51972129), and the National Key Research and Development Program of China (Grant No. 2017YFE0120500), the Key Research and Development Program of Hubei (Grant No. 2020BAB079), and the South Xinjiang Innovation and Development Program of Key Industries of Xinjiang Production and Construction Corps (Grants No. 2020DB002). C.D.W. acknowledges the Hubei "Chu-Tian Young Scholar" program.

Appendix A. Supporting information

Supplementary data associated with this article can be found in the online version at [doi:10.1016/j.apcatb.2022.121322](https://doi.org/10.1016/j.apcatb.2022.121322).

References

- [1] Y. Wang, A. Vogel, M. Sachs, R.S. Sprick, L. Wilbraham, S.J.A. Moniz, R. Godin, M. A. Zwiernburg, J.R. Durrant, A.I. Cooper, J. Tang, Current understanding and challenges of solar-driven hydrogen generation using polymeric photocatalysts, *Nat. Energy* 4 (2019) 746–760.
- [2] J.N. Tiwari, S. Sultan, C.W. Myung, T. Yoon, N. Li, M. Ha, A.M. Harzandi, H. J. Park, D.Y. Kim, S.S. Chandrasekaran, W.G. Lee, V. Vij, H. Kang, T.J. Shin, H. S. Shin, G. Lee, Z. Lee, K.S. Kim, Multicomponent electrocatalyst with ultralow Pt loading and high hydrogen evolution activity, *Nat. Energy* 3 (2018) 773–782.

- [3] D. Zhao, Y. Wang, C.-L. Dong, Y.-C. Huang, J. Chen, F. Xue, S. Shen, L. Guo, Boron-doped nitrogen-deficient carbon nitride-based Z-scheme heterostructures for photocatalytic overall water splitting, *Nat. Energy* 6 (2021) 388–397.
- [4] M. Humayun, C. Wang, W. Luo, Recent progress in the synthesis and applications of composite photocatalysts: a critical review, *Small, Methods* 6 (2021), 2101395.
- [5] Z. Wang, Y. Luo, T. Hisatomi, J.J.M. Vequizo, S. Suzuki, S. Chen, M. Nakabayashi, L. Lin, Z. Pan, N. Kariya, A. Yamakata, N. Shibata, T. Takata, K. Teshima, K. Domen, Sequential cocatalyst decoration on BaTaO₂N towards highly-active Z-scheme water splitting, *Nat. Commun.* 12 (2021) 1005.
- [6] M. Ebihara, T. Ikeda, S. Okunaka, H. Tokudome, K. Domen, K. Katayama, Charge carrier mapping for Z-scheme photocatalytic water-splitting sheet via categorization of microscopic time-resolved image sequences, *Nat. Commun.* 12 (2021) 3716.
- [7] S. Chen, J.J.M. Vequizo, Z. Pan, T. Hisatomi, M. Nakabayashi, L. Lin, Z. Wang, K. Kato, A. Yamakata, N. Shibata, T. Takata, T. Yamada, K. Domen, Surface modifications of (ZnSe)_{0.5}(CuGa_{2.5}Se_{4.25})_{0.5} to promote photocatalytic Z-scheme overall water splitting, *J. Am. Chem. Soc.* 143 (2021) 10633–10641.
- [8] Q. Wang, T. Hisatomi, Q. Jia, H. Tokudome, M. Zhong, C. Wang, Z. Pan, T. Takata, M. Nakabayashi, N. Shibata, Y. Li, I.D. Sharp, A. Kudo, T. Yamada, K. Domen, Scalable water splitting on particulate photocatalyst sheets with a solar-to-hydrogen energy conversion efficiency exceeding 1%, *Nat. Mater.* 15 (2016) 611–615.
- [9] Y. Wang, H. Suzuki, J. Xie, O. Tomita, D.J. Martin, M. Higashi, D. Kong, R. Abe, J. Tang, Mimicking natural photosynthesis: solar to renewable H₂ fuel synthesis by Z-scheme water splitting systems, *Chem. Rev.* 118 (2018) 5201–5241.
- [10] M. Humayun, H. Ullah, M. Usman, A. Habibi-Yangjeh, A.A. Tahir, C. Wang, W. Luo, Perovskite-type lanthanum ferrite based photocatalysts: preparation, properties, and applications, *J. Energy Chem.* 66 (2022) 314–338.
- [11] G. Liao, Y. Gong, L. Zhang, H. Gao, G.-J. Yang, B. Fang, Semiconductor polymeric graphitic carbon nitride photocatalysts: the “holy grail” for the photocatalytic hydrogen evolution reaction under visible light, *Energy Environ. Sci.* 12 (2019) 2080–2147.
- [12] M. Humayun, H. Ullah, A.A. Tahir, A.R. bin Mohd Yusoff, M.A. Mat Teridi, M. K. Nazeeruddin, W. Luo, An overview of the recent progress in polymeric carbon nitride based photocatalysis, *Chem. Rev.* 21 (2021) 1811–1844.
- [13] W.-J. Ong, L.-L. Tan, Y.H. Ng, S.-T. Yong, S.-P. Chai, Graphitic carbon nitride (g-C₃N₄)-based photocatalysts for artificial photosynthesis and environmental remediation: Are we a step closer to achieving sustainability? *Chem. Rev.* 116 (2016) 7159–7329.
- [14] T. Ma, Q. Shen, B.Z.-J. Xue, R. Guan, X. Liu, H. Jia, B. Xu, Facile synthesis of Fe-doped g-C₃N₄ for enhanced visible-light photocatalytic activity, *Inorg. Chem. Commun.* 107 (2019), 107451.
- [15] H. Li, C. Shan, B. Pan, Fe(III)-doped g-C₃N₄ mediated peroxymonosulfate activation for selective degradation of phenolic compounds via high-valent iron-oxo species, *Environ. Sci. Technol.* 52 (2018) 2197–2205.
- [16] D. Chen, K. Wang, W. Hong, R. Zong, W. Yao, Y. Zhu, Visible light photoactivity enhancement via CuTCPP hybridized g-C₃N₄ nanocomposite, *Appl. Catal. B* 166 (2015) 366–373.
- [17] M. Humayun, H. Ullah, L. Shu, X. Ao, A.A. Tahir, C. Wang, W. Luo, Plasmon assisted highly efficient visible light catalytic CO₂ reduction over the noble metal decorated Sr-incorporated g-C₃N₄, *Nano Micro Lett.* 13 (2021) 209.
- [18] W. Zou, X.-H. Liu, C. Xue, X.-T. Zhou, H.-Y. Yu, P. Fan, H.-B. Ji, Enhancement of the visible-light absorption and charge mobility in a zinc porphyrin polymer/g-C₃N₄ heterojunction for promoting the oxidative coupling of amines, *Appl. Catal. B* 285 (2021), 119863.
- [19] X. Zhang, L. Lin, D. Qu, J. Yang, Y. Weng, Z. Wang, Z. Sun, Y. Chen, T. He, Boosting visible-light driven solar-fuel production over g-C₃N₄/tetra(4-carboxyphenyl) porphyrin iron(III) chloride hybrid photocatalyst via incorporation with carbon dots, *Appl. Catal. B* 265 (2020), 118595.
- [20] L. Lin, C. Hou, X. Zhang, Y. Wang, Y. Chen, T. He, Highly efficient visible-light driven photocatalytic reduction of CO₂ over g-C₃N₄ nanosheets/tetra(4-carboxyphenyl)porphyrin iron(III) chloride heterogeneous catalysts, *Appl. Catal. B* 221 (2018) 312–319.
- [21] Z. Fan, M. Bosman, X. Huang, D. Huang, Y. Yu, K.P. Ong, Y.A. Akimov, L. Wu, B. Li, J. Wu, Y. Huang, Q. Liu, C. Eng Png, C. Lip Gan, P. Yang, H. Zhang, Stabilization of 4H hexagonal phase in gold nanoribbons, *Nat. Commun.* 6 (2015) 7684.
- [22] J. Gao, Y. Wang, S. Zhou, W. Lin, Y. Kong, A facile one-step synthesis of Fe-doped g-C₃N₄ nanosheets and their improved visible-light photocatalytic performance, *ChemCatChem* 9 (2017) 1708–1715.
- [23] A. Zada, M. Humayun, F. Raziq, X. Zhang, Y. Qu, L. Bai, C. Qin, L. Jing, H. Fu, Exceptional visible-light-driven cocatalyst-free photocatalytic activity of g-C₃N₄ by well designed nanocomposites with plasmonic Au and SnO₂, *Adv. Energy Mater.* 6 (2016), 1601190.
- [24] L. Zhou, J. Lei, F. Wang, L. Wang, M.R. Hoffmann, Y. Liu, S.-I. In, J. Zhang, Carbon nitride nanotubes with in situ grafted hydroxyl groups for highly efficient spontaneous H₂O₂ production, *Appl. Catal. B* 288 (2021), 119993.
- [25] G. Liu, G. Dong, Y. Zeng, C. Wang, The photocatalytic performance and active sites of g-C₃N₄ effected by the coordination doping of Fe(III), *Chin. J. Catal.* 41 (2020) 1564–1572.
- [26] I. Ahmed, X. Wang, N. Boualili, H. Xu, R. Farha, M. Goldmann, L. Ruhlmann, Photocatalytic synthesis of silver dendrites using electrostatic hybrid films of porphyrin-polyoxometalate, *Appl. Catal. A* 447 448 (2012) 89–99.
- [27] Y. Li, M. Gu, T. Shi, W. Cui, X. Zhang, F. Dong, J. Cheng, J. Fan, K. Lv, Carbon vacancy in C₃N₄ nanotube: electronic structure, photocatalysis mechanism and highly enhanced activity, *Appl. Catal. B* 262 (2020), 118281.
- [28] F. Raziq, Y. Qu, M. Humayun, A. Zada, H. Yu, L. Jing, Synthesis of SnO₂/B-P codoped g-C₃N₄ nanocomposites as efficient cocatalyst-free visible-light photocatalysts for CO₂ conversion and pollutant degradation, *Appl. Catal. B* 201 (2017) 486–494.
- [29] S. Neubert, D. Mitoraj, S.A. Shevlin, P. Pulisova, M. Heimann, Y. Du, G.K.L. Goh, M. Pacia, K. Kruczala, S. Turner, W. Macyk, Z.X. Guo, R.K. Hocking, R. Beranek, Highly efficient rutile TiO₂ photocatalysts with single Cu(ii) and Fe(iii) surface catalytic sites, *J. Mater. Chem. A* 4 (2016) 3127–3138.
- [30] M. Humayun, H. Ullah, J. Cao, W. Pi, Y. Yuan, S. Ali, A.A. Tahir, P. Yue, A. Khan, Z. Zheng, Q. Fu, W. Luo, Experimental and DFT studies of Au deposition over WO₃/g-C₃N₄ Z-scheme heterojunction, *Nano Micro Lett.* 12 (2019) 7.
- [31] F. Raziq, M. Humayun, A. Ali, T. Wang, A. Khan, Q. Fu, W. Luo, H. Zeng, Z. Zheng, B. Khan, H. Shen, X. Zu, S. Li, L. Qiao, Synthesis of S-doped porous g-C₃N₄ by using ionic liquids and subsequently coupled with Au-TiO₂ for exceptional cocatalyst-free visible-light catalytic activities, *Appl. Catal. B* 237 (2018) 1082–1090.
- [32] M. Humayun, W. Pi, Y. Yuan, L. Shu, J. Cao, A. Khan, Z. Zheng, Q. Fu, Y. Tian, W. Luo, A rational design of g-C₃N₄-based ternary composite for highly efficient H₂ generation and 2,4-DCP degradation, *J. Colloid Interface Sci.* 599 (2021) 484–496.
- [33] M. Humayun, Z. Hu, A. Khan, W. Cheng, Y. Yuan, Z. Zheng, Q. Fu, W. Luo, Highly efficient degradation of 2,4-dichlorophenol over CeO₂/g-C₃N₄ composites under visible-light irradiation: Detailed reaction pathway and mechanism, *J. Hazard. Mater.* 364 (2019) 635–644.
- [34] S. Nayak, L. Mohapatra, K. Parida, Visible light-driven novel g-C₃N₄/NiFe-LDH composite photocatalyst with enhanced photocatalytic activity towards water oxidation and reduction reaction, *J. Mater. Chem. A* 3 (2015) 18622–18635.
- [35] J. Xu, Q. Gao, Z. Wang, Y. Zhu, An all-organic 0D/2D supramolecular porphyrin/g-C₃N₄ heterojunction assembled via π - π interaction for efficient visible photocatalytic oxidation, *Appl. Catal. B* 291 (2021), 120059.
- [36] P. Zeng, X. Ji, Z. Su, S. Zhang, WS₂/g-C₃N₄ composite as an efficient heterojunction photocatalyst for biocatalyzed artificial photosynthesis, *RSC Adv.* 8 (2018) 20557–20567.
- [37] K. Zhong, J. Feng, H. Gao, Y. Zhang, K. Lai, Fabrication of BiVO₄@g-C₃N₄(100) heterojunction with enhanced photocatalytic visible-light-driven activity, *J. Solid State Chem.* 274 (2019) 142–151.
- [38] QuantumATK version Q-2019.12, www.quantumatk.com.
- [39] H. Li, H. Yu, X. Quan, S. Chen, Y. Zhang, Uncovering the key role of the Fermi Level of the electron mediator in a Z-scheme photocatalyst by detecting the charge transfer process of WO₃-metal-g-C₃N₄ (Metal = Cu, Ag, Au), *ACS Appl. Mater. Interfaces* 8 (2016) 2111–2119.
- [40] Y. Kang, F. Yu, L. Zhang, W. Wang, L. Chen, Y. Li, Review of ZnO-based nanomaterials in gas sensors, *Solid State Ion.* 360 (2021), 115544.